

Image reconstruction and image quality evaluation for a 64-slice CT scanner with z-flying focal spot

T. G. Flohr^{a)}

*Siemens Medical Solutions, Computed Tomography, Forchheim, Germany
and Department of Diagnostic Radiology, Eberhard-Karls-Universität, Tübingen, Germany*

K. Stierstorfer, S. Ulzheimer, and H. Bruder

Siemens Medical Solutions, Computed Tomography, Forchheim, Germany

A. N. Primak and C. H. McCollough

Department of Radiology, Mayo Clinic College of Medicine, Rochester, Minnesota 55905

(Received 15 December 2004; revised 6 May 2005; accepted for publication 19 May 2005; published 21 July 2005)

We present a theoretical overview and a performance evaluation of a novel z-sampling technique for multidetector row CT (MDCT), relying on a periodic motion of the focal spot in the longitudinal direction (z-flying focal spot) to double the number of simultaneously acquired slices. The z-flying focal spot technique has been implemented in a recently introduced MDCT scanner. Using 32×0.6 mm collimation, this scanner acquires 64 overlapping 0.6 mm slices per rotation in its spiral (helical) mode of operation, with the goal of improved longitudinal resolution and reduction of spiral artifacts. The longitudinal sampling distance at isocenter is 0.3 mm. We discuss in detail the impact of the z-flying focal spot technique on image reconstruction. We present measurements of spiral slice sensitivity profiles (SSPs) and of longitudinal resolution, both in the isocenter and off-center. We evaluate the pitch dependence of the image noise measured in a centered 20 cm water phantom. To investigate spiral image quality we present images of an anthropomorphic thorax phantom and patient scans. The full width at half maximum (FWHM) of the spiral SSPs shows only minor variations as a function of the pitch, measured values differ by less than 0.15 mm from the nominal values 0.6, 0.75, 1, 1.5, and 2 mm. The measured FWHM of the smallest slice ranges between 0.66 and 0.68 mm at isocenter, except for pitch 0.55 (0.72 mm). In a centered z-resolution phantom, bar patterns up to 15 lp/cm can be visualized independent of the pitch, corresponding to 0.33 mm longitudinal resolution. 100 mm off-center, bar patterns up to 14 lp/cm are visible, corresponding to an object size of 0.36 mm that can be resolved in the z direction. Image noise for constant effective mAs is almost independent of the pitch. Measured values show a variation of less than 7% as a function of the pitch, which demonstrates correct utilization of the applied radiation dose at any pitch. The product of image noise and square root of the slice width (FWHM of the respective SSP) is the same constant for all slices except 0.6 mm. For the thinnest slice, relative image noise is increased by 17%. Spiral windmill-type artifacts are effectively suppressed with the z-flying focal spot technique, which has the potential to maintain a low artifact level up to pitch 1.5, in this way increasing the maximum volume coverage speed that can be clinically used. © 2005 American Association of Physicists in Medicine. [DOI: 10.1118/1.1949787]

Key words: cone-beam CT, multi-detector row CT, CT image quality evaluation, CT data sampling

I. INTRODUCTION

Clinical applications benefit from multidetector row CT (MDCT) technology in several ways:¹⁻⁴

- (1) Shorter scan time [important for trauma victims, patients with limited ability to cooperate, pediatric cases, multi-phase exams, and CT angiography (CTA)].
- (2) Extended scan range (important for CTA or combined chest-abdomen-pelvis scans such as in oncological staging).
- (3) Improved longitudinal resolution (beneficial for all reconstructions, in particular when three-dimensional postprocessing is part of the clinical protocol).

Most protocols can benefit from a combination of these advantages. Meanwhile, 16-slice CT systems have been established in clinical practice, and isotropic submillimeter coverage of extended anatomical ranges has become the clinical standard for many applications.^{5,6} Insufficient volume coverage speed, which was a serious problem in the days of single-slice CT,⁷ only rarely becomes a limiting factor with 16-slice CT. In the light of this performance level, the potential clinical benefits from a further technical development of MDCT have to be carefully considered. Clinical progress can more likely be expected from further improvements in spatial and temporal resolution rather than from a mere increase in the volume coverage speed, which will be

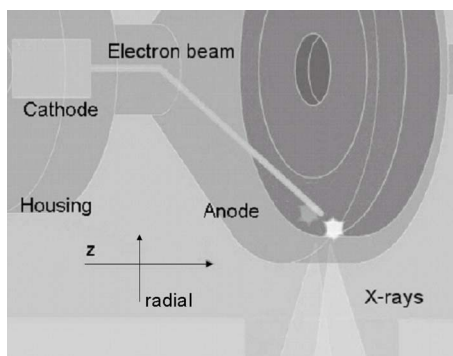


FIG. 1. Principle of the z-flying focal spot technique, illustrated for the example of a rotating envelope tube. The entire tube housing rotates in an oil bath, and the anode plate is in direct contact with the cooling oil. By permanent electromagnetic deflection of the electron beam the focal spot is wobbled between two different positions on the anode plate (indicated by two asterisks). Due to the anode angle of typically 7° – 9° this translates into a motion both in the radial direction and in the z direction.

beneficial for a limited spectrum of applications, such as pure arterial CTAs of the carotid arteries and the circle of Willis or thorax examinations in emergency cases (acute pulmonary embolism, aortic dissections). For ECG-gated cardiac scanning, improved longitudinal resolution is of key importance for the reliable characterization of coronary plaques and wall changes.^{8,9} Even with 16-slice CT, stents or severely calcified arteries are often difficult to image, which so far has prevented the successful integration of CT coronary angiography into routine clinical algorithms.

In this paper, we discuss a novel acquisition scheme for MDCT data, which makes use of a periodic motion of the focal spot in the longitudinal direction (z direction) to double the number of simultaneously acquired slices with the goal of improved longitudinal resolution and reduction of spiral artifacts.¹⁰ The motion of the focal spot can be realized by an electromagnetic deflection unit (z-flying focal spot). The new acquisition scheme has been implemented in a recently introduced MDCT scanner (SOMATOM Sensation 64, Siemens AG, Forchheim, Germany), which acquires 64 overlapping 0.6 mm slices with a detector collimation of 32×0.6 mm. We discuss the impact of the z-flying focal spot technique on image reconstruction and investigate image quality. Finally, we show the potential clinical impact of this new z-sampling technology.

II. MATERIALS AND METHODS

A. Principles of the z-flying focal spot technology

The z-flying focal spot technology for MDCT spiral scanning makes use of a periodic motion of the focal spot in the longitudinal direction to improve data sampling along the z axis.¹⁰ By continuous electromagnetic deflection of the electron beam in the x-ray tube the focal spot is wobbled between two different positions on the anode plate. Due to the anode angle of typically 7° – 9° , this translates into a motion both in the radial direction and in the z direction (Fig. 1). The radial motion is a side-effect which has to be taken care of by

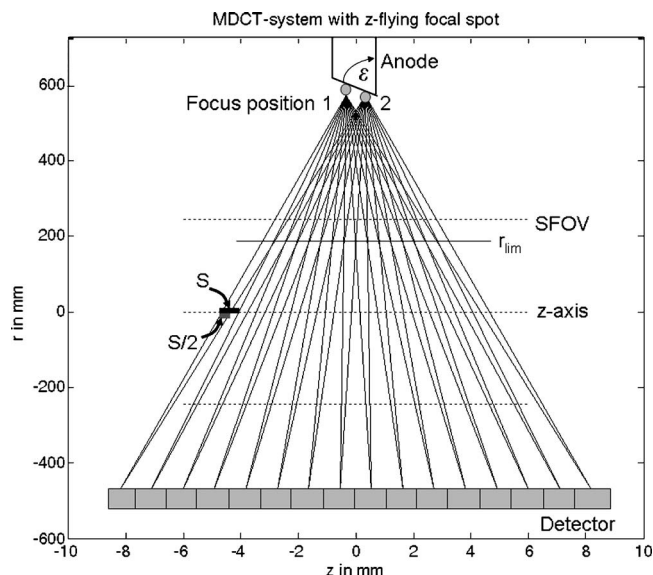


FIG. 2. Schematic illustration of improved z-sampling with the z-flying focal spot technique. Two subsequent M -slice readings are shifted by half a collimated slice-width $S/2$ at iso-center and can be interleaved to one $2M$ -slice projection. Improved z-sampling is not only achieved at iso-center, but maintained in a wide range of the scan field of view (SFOV), which can be defined by a “limiting” radius r_{lim} . The distances of both focal spot and detector, from the iso-center, and the widths of the detector rows are true to scale for the evaluated CT scanner. For the sake of clearness only $M=16$ detector rows are shown. The evaluated CT system uses $M=32$ detector rows in combination with the z-flying focal spot.

the image reconstruction algorithms (see Sec. II B). The amplitude of the periodic z motion is adjusted in a way that two subsequent readings are shifted by half a collimated slice width in the patient’s longitudinal direction at isocenter (Fig. 2). Therefore, the measurement rays of two subsequent readings with collimated slice-width S interleave in the z direction, and every two M -slice readings are combined to one $2M$ -slice projection with a sampling distance of $S/2$ at iso-center (Fig. 2). The pitch-independent z-sampling grid $\Delta z = S/2$ fulfills the Nyquist sampling theorem and allows improved longitudinal resolution by using narrow spiral interpolation functions and the suppression of spiral artifacts. Typical spiral artifacts present as hyper- or hypo-dense “windmill” structures surrounding z -inhomogeneous high-contrast objects such as bones, which rotate when scrolling through a stack of images. They are caused by the spiral interpolation as a consequence of insufficient data sampling in the z direction.¹¹

The evaluated CT scanner uses an adaptive array detector, which comprises detector rows with different sizes in the longitudinal direction. It consists of 40 detector rows, the 32 central rows having a 0.6 mm collimated slice width and the 4 outer rows on both sides having a 1.2 mm collimated slice width, both measured at the isocenter of the scanner. The total coverage in the longitudinal direction (z direction) is 28.8 mm (Fig. 3). By proper combination of the signals of the individual detector rows, the collimations 32×0.6 and 24×1.2 mm (in the isocenter) can be realized. Using the z-flying focal spot technique, two subsequent 32-slice read-

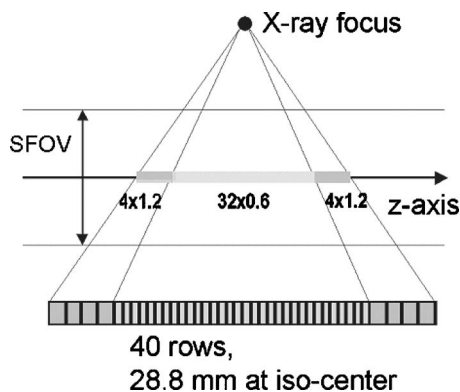


FIG. 3. Schematic drawing of the adaptive array detector used in the CT scanner evaluated.

ings with 0.6 mm collimated slice width are combined to one 64-slice projection with a sampling distance of 0.3 mm at isocenter. In this way 64 overlapping 0.6 mm slices per rotation are acquired, and the adaptive multiple plane reconstruction (AMPR) algorithm^{12,13} is used for image reconstruction. The AMPR approach is an extension and generalization of the Advanced Single Slice Rebinning (ASSR) algorithm,^{14–16} which belongs to the class of Nutating Slice Reconstruction (NSR) algorithms. Unlike ASSR, AMPR allows for a free selection of the spiral pitch with optimized dose utilization, which is beneficial for medical applications. A detailed algorithmic description of AMPR may be found in Ref. 13, hence it will not be repeated here.

B. Impact of the z-flying focal spot on image reconstruction and basic system parameters

With a flying focal spot in z direction the focus moves not only in z but, due to the flat anode angle of the x-ray tube, also in radial direction (Fig. 1). In our approach, this radial movement is taken into account in the interpolation (rebinning) from fan beam to parallel data, which are used as an input for the AMPR algorithm.¹³ The flying focal spot technology is used for spiral (helical) operation modes only.

We assume that the focal spot and multirow detector are fixed with respect to each other (third-generation CT system). Note that the focus-isocenter distance R_F^r depends on the reading number r as a consequence of the periodic motion of the focal spot. Each individual measurement ray is characterized by its reading (view) angle α_r , its fan angle β_k^r within reading r , and by its slice index m (M is the number of detector rows). In our notation, k is the index of the detector channel. The logarithmic attenuation values, i.e., the line integrals of the object's attenuation coefficient μ along the measured rays are denoted by $f(\alpha_r, \beta_k^r, m)$. The CT scanner evaluated has $N_k=672$ detector channels per row. The number of detector rows is either $M=32$ (with 32×0.6 mm collimation) or $M=24$ (with 24×1.2 mm collimation). The z -flying focal spot is only used for 32×0.6 mm collimation. The design of the x-ray tube does not allow sufficient radial displacement of the focal spot for 24×1.2 mm collimation. The CT scanner operates in two different modes. The first

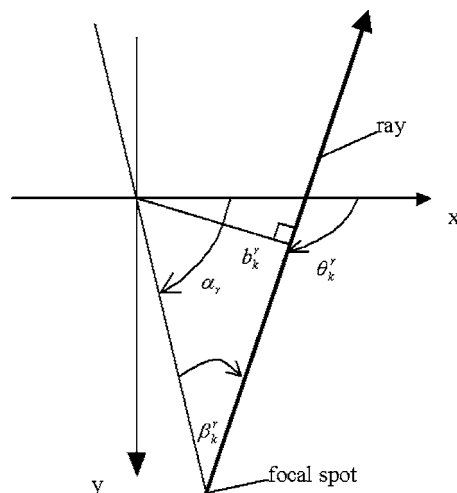


FIG. 4. Definition of the scanner geometry. The z (longitudinal) axis points into the plane of the diagram.

one, which is used for 0.33, 0.375, and 0.5 s gantry rotation time, is a mode with quarter detector offset and z -flying focal spot. Up to $N_r=2320$ readings per full rotation are acquired. The second mode, which is used for 1.0 s gantry rotation time, combines an eighth detector offset with both in-plane (ϕ) flying focal spot and z -flying focal spot. $N_r=4640$ readings per full rotation are acquired. The scanner geometry is defined in Fig. 4. The basic rebinning equations from fan beam to parallel geometry are

$$\begin{aligned}\theta_k^r &= \alpha_r + \beta_k^r, \\ b_k^r &= R_F^r \sin \beta_k^r,\end{aligned}\quad (1)$$

θ_k^r is the azimuthal angle and b_k^r denotes the distance of a ray from the isocenter. Note that in the case where we use a z movement of the focus, the fan angle β_k^r is no longer equidistantly distributed since the focus-isocenter distance R_F^r depends on the reading number. We will now derive formulas for α_r , β_k^r , and R_F^r . The two types of focus movement (z -flying focal spot and combined in-plane/ z -flying focal spot) are illustrated in Fig. 5.

Let us first consider a stationary gantry and $\alpha_r=0$. In this case the (virtual) central focus position is aligned with the x

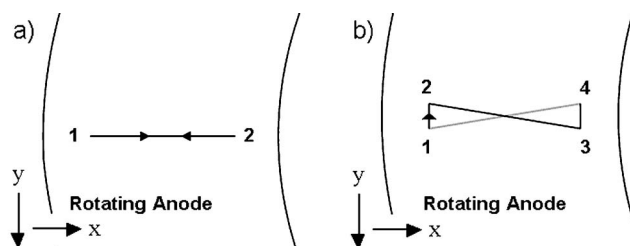


FIG. 5. Illustration of the focus path on the anode plate for the two types of focus movement used in the CT scanner evaluated: z -flying focal spot (a) and combined in-plane and z -flying focal spot (b), see also Fig. 2. For the selected projection angle ($\alpha_r=0$, see Fig. 4) the (virtual) central focus position is aligned with the x axis, which is the radial direction. The angular direction is given by y .

axis, which is the radial direction. The angular direction is given by y , and focus position \mathbf{f}^p and detector element positions \mathbf{d}_k are

$$\mathbf{f}^p = \begin{pmatrix} x_F(0) \\ y_F(0) \end{pmatrix} = \begin{pmatrix} R_F + \delta R^p \\ \delta a^p \end{pmatrix},$$

$$\mathbf{d}_k = \begin{pmatrix} x_D(\beta_k^0) \\ y_D(\beta_k^0) \end{pmatrix} = \begin{pmatrix} R_F - R_{FD} \cos \beta_k^0 \\ -R_{FD} \sin \beta_k^0 \end{pmatrix}, \quad (2)$$

$$\rho = 0 \dots 1 \dots N_{\text{ffs}} - 1, \quad k = 0 \dots 1 \dots N_k - 1,$$

where N_{ffs} is the number of positions in the periodical focal spot movement and N_k is the number of detector elements. R_F is the nominal focus-isocenter distance (without flying focal spot), R_{FD} is the nominal focus-detector distance. In the evaluated CT system, $R_F = 570$ mm and $R_{FD} = 1060$ mm. We have neglected the z component of the vectors which is not relevant for the rebinning procedure. The focal spot deviations in x (radial) and y (angular) directions in reading r are given by the quantities δR^p and δa^p tabulated in the following

Combined phi/z flying focal spot
(1.0 s rotation)

ρ	0	1	2	3
δR^p	$- \delta R $	$- \delta R $	$+ \delta R $	$+ \delta R $
δa^p	$+ \delta a $	$- \delta a $	$+ \delta a $	$- \delta a $

z flying focal spot
(0.33 s; 0.375 s; 0.5 s)

ρ	0	1
δR^p	$- \delta R $	$+ \delta R $
δa^p	0	0

with

$$|\delta R| = \frac{R_{FD} S}{4(R_{FD} - R_F) \tan \epsilon}, \quad (3)$$

$$|\delta a| = \frac{R_{FD} R_F \sin \Delta \beta}{4(R_{FD} - R_F)},$$

where ϵ is the anode angle and $\Delta \beta$ is the fan angle increment. S is the collimated slice width of a detector row. Note that with $|\delta R|$ as defined in Eq. (3) the two projected z positions of the flying focal spot are

$$\Delta z = 2 \delta R \tan \epsilon = \frac{R_{FD}}{(R_{FD} - R_F) 2} S \quad (4)$$

apart. As a consequence of the geometrical magnification this corresponds to a z shift of

$$\frac{(R_{FD} - R_F)}{R_{FD}} \Delta z = \frac{S}{2}$$

(half the collimated slice width of one detector row) in the isocenter of the scanner, which was intended in the design of the z -flying focal spot technique.

Interleaving of the data in the z direction is perfect at isocenter, but less optimal with increasing radial distance from the isocenter. The benefits of the z -flying focal spot technique are maintained within a “limiting” radius r_{lim} , which can be defined as the radial distance of the intersection points of the rays measured by adjacent detector channels at z positions 1 and 2 of the focal spot (see Fig. 2). Using simple geometric relations, r_{lim} is given by

$$\frac{r_{\text{lim}}}{S/2} = \frac{R_{FD} - R_F + r_{\text{lim}}}{SR_{FD}/R_F} \rightarrow r_{\text{lim}} = \frac{R_F(R_{FD} - R_F)}{2R_{FD} - R_F}. \quad (5)$$

Inserting $R_F = 570$ mm and $R_{FD} = 1060$ mm into Eq. (5), we obtain $r_{\text{lim}} = 180$ mm. The scan field of view defined by the limiting radius (360 mm) corresponds well to the area of interest for the majority of medical CT applications.

Due to the finite aperture of the detector elements in the z direction, the measurement data are low-pass filtered with a rectangle of width S at isocenter. Additional low-pass filtering is introduced by the finite length of the focal spot in the z direction. Therefore, even imperfect z -interleaving close to or outside the limiting radius will not introduce artifacts but rather decrease resolution.

For modes with z -flying focal spot alone the nominal fan angle of channel k is

$$\beta_k^0 = (k - 334.25) \Delta \beta \quad (6)$$

(1/4 detector offset). For modes with combined in-plane/ z -flying focal spot the nominal fan angle of channel k is

$$\beta_k^0 = (k - 334.375) \Delta \beta \quad (7)$$

(1/8 detector offset). From the vectors \mathbf{f} and \mathbf{d}_k of Eq. (2), although derived for $\alpha_r = 0$, the fan angle for channel k in any reading r (characterized by the focal spot position $\rho(r) \equiv r \bmod N_{\text{ffs}}$) can be calculated as follows:

$$\beta_k^r = \text{angle}(-\mathbf{f}^{\rho(r)}, \mathbf{d}_k - \mathbf{f}^{\rho(r)}), \quad (8)$$

where the angle between two (two-dimensional) vectors is given by

$$\text{angle}(\mathbf{x}, \mathbf{y}) = \text{asin} \frac{(\mathbf{x} \times \mathbf{y})_3}{|\mathbf{x}| |\mathbf{y}|} = \text{asin} \frac{x_1 y_2 - x_2 y_1}{\sqrt{x_1^2 + x_2^2} \sqrt{y_1^2 + y_2^2}}. \quad (9)$$

(Here, \times denotes the vector cross product). Similarly, the focus angle (projection angle) of reading r is

$$\alpha^r = \alpha_0^r + \delta \alpha^{\rho(r)} \quad \text{with } \rho(r) \equiv r \bmod N_{\text{ffs}}, \quad (10)$$

where the nominal focus position (stationary focus) moves according to

$$\alpha_0^r = r \Delta\alpha = r \frac{2\pi}{N_r}, \quad (11)$$

and the deviation to the nominal focus position (flying focal spot) is

$$\delta\alpha^\rho = \text{angle}\left(\begin{pmatrix} R_F \\ 0 \end{pmatrix}, \mathbf{f}^\rho\right). \quad (12)$$

The focus radius in focus position ρ is given by

$$R_F^\rho = \sqrt{(R_F + \delta R^\rho)^2 + (\delta\alpha^\rho)^2}. \quad (13)$$

The rebinning is now performed in two steps. First, following the first of the rebinning equations (1), each of the focus positions ρ is rebinned separately to obtain an intermediate stream of vectors (θ_k^r, β_k^r) . In doing so, the true focus angles of Eq. (10) are taken into account and the resulting grid in θ is chosen equidistantly. The azimuthal angles θ_k^r are identical for all focus positions ρ . The sampling distance in θ direction is

$$\Delta\theta = 2\Delta\alpha = \frac{4\pi}{N_r} \quad (14)$$

for modes with z-flying focal spot but without in-plane flying focal spot, and

$$\Delta\theta = 4\Delta\alpha = \frac{8\pi}{N_r} \quad (15)$$

for modes with combined in-plane/z-flying focal spot.

Second, the second rebinning equation (1) is used to rebin all data vectors to a common equidistant b grid using the true (nonequidistant) fan angles β_k^r of Eq. (8). The desired sampling distance in b direction is

$$\Delta b = R_F \sin(\Delta\beta/2). \quad (16)$$

Now the data are in parallel geometry, with a common equidistant b grid, and can be interleaved in z direction to obtain an effective data set of twice the number of rows.

With the CT scanner investigated, parallel projections with $2M=64$ rows (sampling distance $S/2$ at isocenter) and $2N_k=1344$ samples are used as an input for the AMPR approach as described in Ref. 13. For the spiral interpolation within the AMPR, a triangle with minimum base width S is used (linear spiral interpolation), and the intermediate image planes are characterized by a SSP with full width at half maximum (FWHM) $\sim S$. Hence, narrow, well-defined slice sensitivity profiles (SSPs) can be established in the subsequent image z -reformation step. A variety of different slice widths are available for retrospective image reconstruction. With 32×0.6 mm collimation and z-flying focal spot, the slice widths $S_{\text{nom}}=0.6, 0.75, 1, 1.5, 2, 3, 4, 5, 6, 7, 8$, and 10 mm may be selected on the user-interface. In the following, we refer to these slice widths, which are defined as the desired FWHM of the spiral SSP, as “nominal” slice widths. The spiral pitch p is freely selectable in the range $0.4 \leq p \leq 1.5$. For wide slices relative to the collimation, the maximum pitch 2 is available. The weighting functions for image z -reformation are chosen such as to maintain constant

FWHM of the spiral SSP independent of the pitch. The widths of the weighting functions vary slightly as a function of the pitch in order to keep the FWHM of the desired slice constant. For all slice widths, the AMPR approach is used for image reconstruction, deviating from the 16-slice CT system evaluated previously.¹³

C. Evaluation of the z-flying focal spot technology: Slice sensitivity profiles, longitudinal resolution, image noise, and spiral image quality

The z-flying focal spot technology was evaluated for a recently introduced MDCT system (SOMATOM Sensation 64, Siemens, Forchheim, Germany). To determine spiral SSPs, we scanned a thin gold plate (40 μm thick) embedded in a Lucite cylinder with 32×0.6 mm collimation in a 64 slice acquisition mode using the z-flying focal spot. The gantry rotation time was 0.5 s, and scan data were acquired at pitch $p=0.5, 0.55, 0.75, 0.85, 0.95, 1, 1.15, 1.25, 1.5$. The gold plate was placed both close to the isocenter of the scanner and 120 mm off-center. Highly overlapping images with an increment of 0.1 mm were reconstructed with the AMPR algorithm for different nominal slice widths (0.6, 0.75, 1.0, 1.5, 2 mm). The reconstruction range was large enough to fully cover the gold plate, i.e., in the first and in the last image the gold plate had completely disappeared and only the Lucite cylinder was visible. For each of the overlapping images, the mean CT value in a small region of interest within the gold plate was determined, and the “background” CT value (CT value of the Lucite cylinder without gold plate) was subtracted. The maximum of these corrected mean values (with the gold plate fully in the reconstructed slice) was normalized to 1. The normalized mean values, plotted as a function of the z positions of the respective image slices, represent the measured SSP. The FWHM of this SSP is the measured slice width. For the nominal 0.6, 0.75, 1.0, and 1.5 mm slices Fourier transforms of the measured SSPs were performed to evaluate the modulation transfer functions (MTFs) in the z direction.

To investigate the maximum achievable longitudinal resolution as a function of the spiral pitch, we used the high-resolution insert of the CATPHAN (The Phantom Laboratories, Salem, NY), originally intended for in-plane resolution measurements, as a z -resolution phantom. For this purpose we turned the high-resolution insert by 90° and aligned the bar patterns in a way that the grids with 12, 13, 14, 15, and 16 lp/cm, corresponding to 0.42, 0.38, 0.36, 0.33, and 0.31 mm resolution, were roughly perpendicular to the z direction. The grid with 15 lp/cm was exactly orthogonal to the z direction. The bar patterns were scanned both at isocenter, 50 mm off-center and 100 mm off-center, at pitch $p=0.5, 0.95$, and 1.45. We used 32×0.6 mm collimation in a 64-slice acquisition mode with z-flying focal spot and reconstructed images with the sharp body-kernel B70 for maximum in-plane resolution. The reconstruction slice-width was 0.6 mm with 0.1 mm reconstruction increment. Longitudinal resolution was visually determined on MPRs in the z direction.

To compare SSPs and longitudinal resolution to the case without z-flying focal spot we reconstructed data of the gold plate phantom and the high resolution insert of the CATPHAN, acquired at pitch 0.53 and 1.375, with a modified approach considering only projections at one z position of the z-flying focal spot. This corresponds reasonably well to evaluating 32-slice spiral data acquired without z-flying focal spot.

We measured image noise in a centered 20 cm water phantom, both in a central region of interest (ROI) and in a small ROI at the periphery of the phantom, at pitch $p=0.5$, 0.55, 0.75, 0.85, 1, 1.15, 1.25, 1.45, 1.5. We used 32×0.6 mm collimation in a 64 slice acquisition mode with z-flying focal spot and 0.5 s gantry rotation time and applied the same effective mAs (120 kV, 100 effective mAs) to all scans. The tube current was automatically adapted from 100 mA at $p=0.5$ to 300 mA at $p=1.5$ to provide constant dose at any spiral pitch p . We measured the average image noise for $S_{\text{nom}}=0.6, 1, 1.5, 2, 5$, and 10 mm nominal slice width as indicated on the user-interface of the CT scanner evaluated. All images were reconstructed with the standard body-kernel B40.

We used both phantom scans and patient data to investigate the influence of the z-flying focal spot technology on spiral image quality. All scans were performed with 32×0.6 mm collimation in a 64 slice acquisition mode with z-flying focal spot and reconstructed at 0.6 mm nominal slice width. To evaluate image quality as a function of the spiral pitch we scanned an anthropomorphic thorax phantom at pitch 0.5, 1.0, and 1.5 (gantry rotation time 0.5 s). To explicitly point out the image quality difference with and without z-flying focal spot we reconstructed patient data (head and neck scan, thorax scan, both at pitch 1.5 with 0.375 s gantry rotation time) twice, on the one hand with the original image reconstruction implemented in the CT scanner investigated, on the other with a modified approach considering only projections at one z position of the z-flying focal spot.

III. RESULTS

A. Slice sensitivity profiles

Figure 6 shows measured SSPs (at isocenter) of the nominal 0.6, 0.75, 1.0, and 1.5 mm slices at pitch 0.95. The SSPs are symmetrical, bell-shaped curves without far-reaching tails that would degrade longitudinal resolution. The 0.6 mm slice in particular is well-defined and compact. The measured FWHMs are 0.67, 0.81, 1.06, and 1.51 mm, respectively. Figure 7 shows the Fourier transforms of the measured SSPs, which are the MTFs in the z direction. The 2% value of the MTF for the thinnest slice (measured FWHM=0.67 mm) is 15.9 lp/cm, hence it can be expected that high-contrast objects down to $1/(2 \times 15.9)$ mm=0.31 mm in size should be separable in the longitudinal direction if the radiation dose is sufficient. The theoretical limit of longitudinal resolution is determined by the active detector aperture in the z direction (0.556 mm at isocenter for the CT-scanner evaluated). This corresponds to a cut-off frequency of $1/(0.556 \text{ cm})=18$ lp/cm, which is equivalent to 0.28 mm resolution.

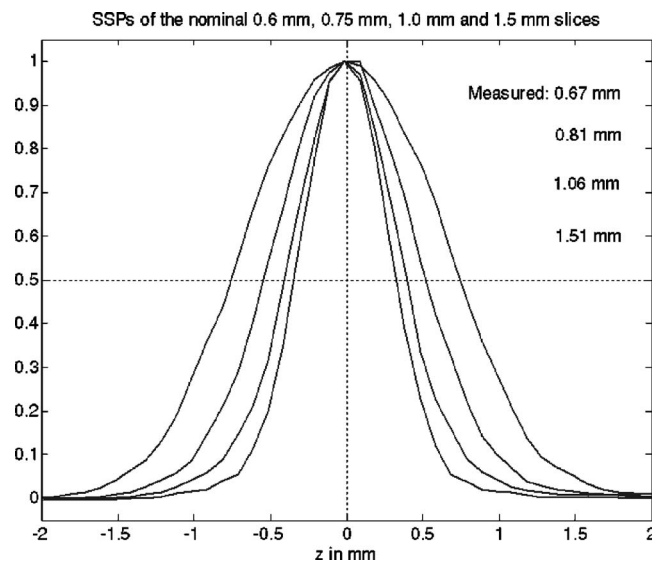


Fig. 6. Measured SSPs at isocenter of the nominal 0.6, 0.75, 1.0, and 1.5 mm slices at pitch 0.95. The measured FWHMs are 0.67, 0.81, 1.06, and 1.51 mm, respectively.

Figure 8 demonstrates that the measured FWHMs of the spiral SSPs at isocenter are almost independent of the pitch, with deviations of less than 0.15 mm from the nominal values. The theoretical FWHM of the smallest slice (0.6 mm) is about 0.63 mm, with measured values ranging between 0.66 and 0.68 mm except for pitch 0.55 (0.72 mm). For the nominal 0.75 mm slice the measured values range between 0.79 and 0.82 mm. For clinical applications, the slice width is important not only in the isocenter of the scanner but also off-center. Figure 9 shows the FWHM of the spiral SSPs at

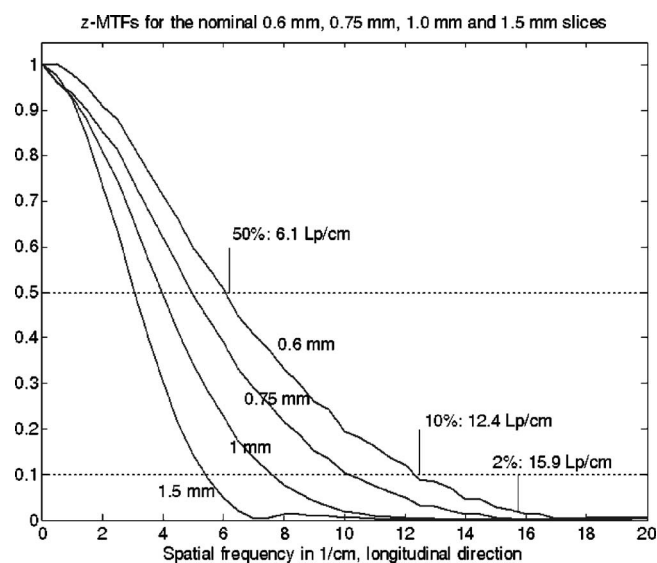


Fig. 7. Fourier transforms of the measured SSPs of the nominal 0.6, 0.75, 1.0, and 1.5 mm slices at pitch 0.95 (see Fig. 6), which are equivalent to the modulation transfer functions (MTF) in the z direction. For the thinnest slice (FWHM=0.67 mm), the 50% value of the MTF is 6.1 lp/cm, the 10% value is 12.4 lp/cm and the 2% value is 15.9 lp/cm, hence it can be expected that high-contrast objects down to 0.31 mm in size should be separable in the longitudinal direction.

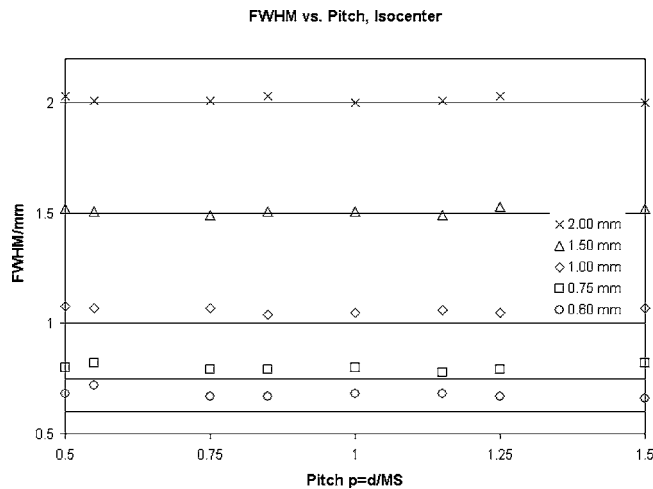


FIG. 8. Measured FWHM of the nominal 0.6, 0.75, 1, 1.5, and 2 mm slices in the isocenter as a function of the spiral pitch. Scan data have been acquired with 32×0.6 mm collimation in a 64-slice acquisition mode using the z-flying focal spot. For the evaluated CT scanner, the slice width is independent of the pitch.

120 mm distance from the isocenter as a function of the pitch. Off-center, the slices are only slightly wider, with a variation between 0.72 and 0.83 mm for the nominal 0.6 mm slice, and between 0.84 and 0.96 mm for the nominal 0.75 mm slice. It can therefore be expected that longitudinal resolution is not severely degraded for off-center objects.

For comparison we also calculated SSPs with a modified reconstruction approach considering only projections at one z position of the focal spot. We chose pitch 0.531 25 (approximated by pitch 0.53 at our scanner) and pitch 1.375 for the evaluation. Using pitch 0.53 complementary data acquired in subsequent rotations interleave in the z direction. Improved z sampling with sampling distance $S/2$ is achieved close to iso-center, and a SSP similar to the case with z-flying focal spot can be established using narrow spiral interpolation

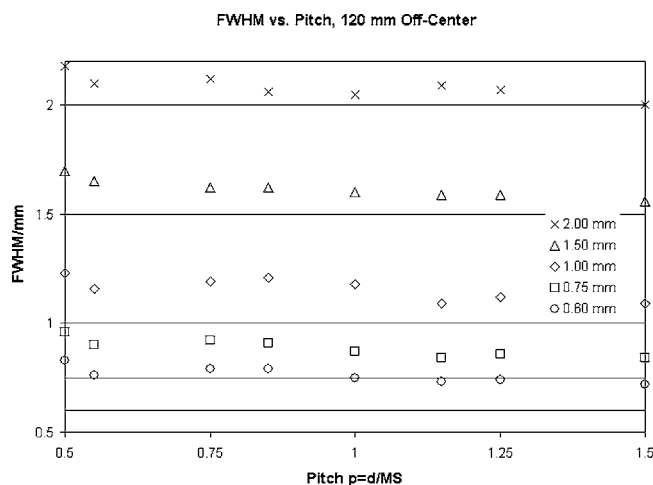


FIG. 9. Measured FWHM of the nominal 0.6, 0.75, 1, 1.5, and 2 mm slices 120 mm off-center as a function of the spiral pitch. Off-center, the slices are only slightly wider (compare to Fig. 8), hence it can be expected that longitudinal resolution is not severely degraded.

SSPs without z-FFS, at pitch 0.53 and 1.38

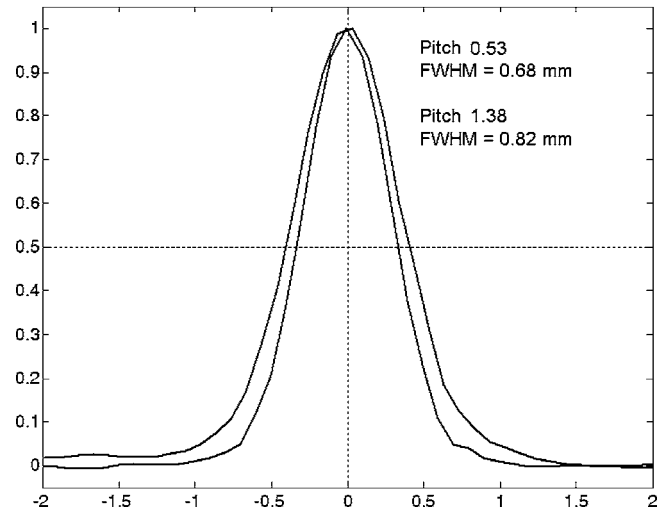


FIG. 10. Measured SSPs at isocenter of the nominal 0.6 mm slice at pitch 0.53 and 1.375 with a modified reconstruction approach considering only projections at one z position of the focal spot (simulating data acquisition without z-flying focal spot). At pitch 0.53 complementary data acquired in subsequent rotations interleave in the z direction. Improved z sampling with sampling distance $S/2$ is achieved close to isocenter, and a SSP similar to the case with z-flying focal spot can be established. At pitch 1.375 there is no interleaving at isocenter, the sampling distance equals S , and the SSP widens up. Consequently, the SSPs of the thinnest slice that can be reconstructed have a FWHM of 0.68 mm at pitch 0.53 (which is similar to the z-flying focal spot case), whereas FWHM=0.82 mm at pitch 1.375.

functions. Using pitch 1.375 there is no interleaving at iso-center, and the sampling distance equals S . Figure 10 shows SSPs at iso-center for the two cases without z-flying focal spot. At pitch 0.53, FWHM=0.68 mm, quite comparable to the thinnest slice that can be achieved with z-flying focal spot. At pitch 1.375, the thinnest slice that can be reconstructed has FWHM=0.82 mm as a consequence of the coarse z-sampling without z-flying focal spot.

B. Longitudinal resolution

Figure 11 shows MPRs of the z-resolution phantom (high-resolution insert of the CATPHAN, turned by 90°) in the isocenter of the scanner, as a function of the pitch. Independent of the pitch all bar patterns up to 16 lp/cm can be visualized. Since the bar patterns with 15 lp/cm are exactly orthogonal to the z axis we conclude that 15 lp/cm, corresponding to 0.33 mm object size, can be resolved in the longitudinal direction independent of the pitch. This is in good agreement with the evaluation of the z-MTF curve for 0.6 mm slice-width, see Fig 7. Pitch-independent improvement of the longitudinal resolution by optimized z sampling was intended in the design of the z-flying focal spot technology. Figure 12 shows MPRs of the z-resolution phantom at pitch 0.95, with the phantom placed in the isocenter, 50 mm off-center and 100 mm off-center. Longitudinal resolution is only slightly degraded for the off-center positions. 100 mm off-center, the bar patterns corresponding to 15 lp/cm are

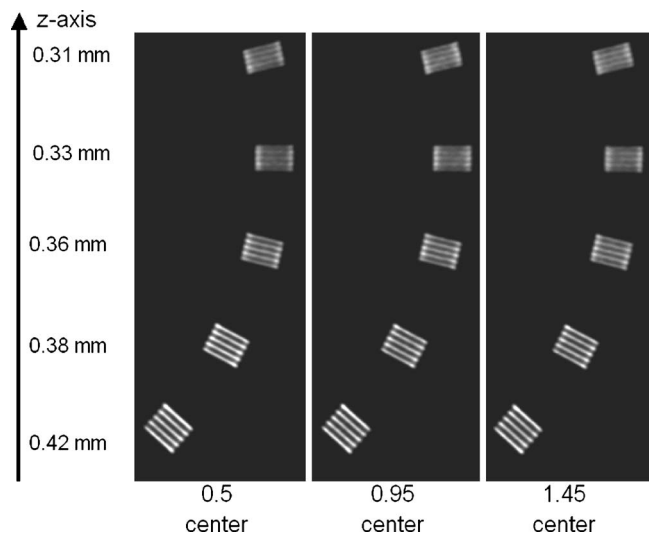


FIG. 11. MPRs of the z-resolution phantom (high-resolution insert of the CATPHAN, the Phantom Laboratories, Salem, NY, turned by 90°) in the isocenter of the scanner as a function of the pitch. Scan data have been acquired with 32×0.6 mm collimation in a 64-slice acquisition mode using the z-flying focal spot and reconstructed with the narrowest slice width (nominal 0.6 mm) and a sharp body kernel (B70). Independent of the pitch all bar-patterns up to 16 lp/cm can be visualized. The bar patterns with 15 lp/cm are exactly perpendicular to the z axis, corresponding to 0.33 mm longitudinal resolution.

somewhat blurred, yet separable. 14 lp/cm are clearly visible, and we conclude that 14 lp/cm, corresponding to an object size of 0.36 mm, can be resolved.

Figure 13 shows MPRs of the z-resolution phantom at isocenter, obtained with a modified reconstruction approach considering only projections at one z position of the focal spot. At pitch 0.53, longitudinal resolution is comparable to the case with z-flying focal spot (see Fig. 11), as a consequence of the improved z-sampling with sampling distance

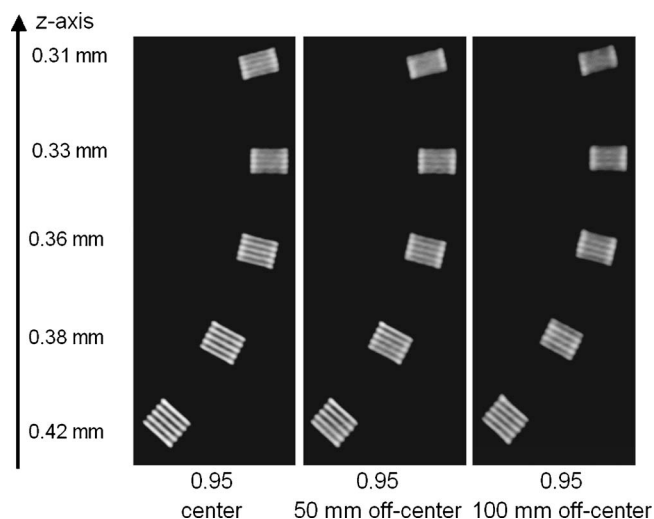


FIG. 12. MPR of the z-resolution phantom at pitch 0.95, positioned in the isocenter, 50 mm off-center and 100 mm off-center. 100 mm off-center, longitudinal resolution is only slightly degraded (14 lp/cm, corresponding to 0.36 mm).

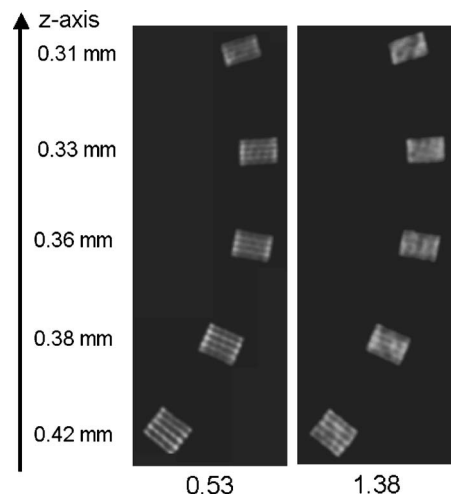


FIG. 13. MPRs of the z-resolution phantom at isocenter, obtained with a modified reconstruction approach considering only projections at one z position of the focal spot (simulating data acquisition without z-flying focal spot). At pitch 0.53, longitudinal resolution is comparable to the case with z-flying focal spot. At pitch 1.375, longitudinal resolution degrades compared to the case with z-flying focal spot (see Fig. 11).

$S/2$ using complementary rays. At pitch 1.375, longitudinal resolution degrades compared to the case with z-flying focal spot (see Fig. 11).

C. Image noise

In Fig. 14, the average image noise σ in the center of a centered 20 cm water phantom is shown as a function of the pitch for constant effective mAs (mAs/pitch) and several nominal slice widths as indicated on the user-interface of the CT scanner investigated. The image noise σ has been arbitrarily normalized to the value at 1 mm slice width and pitch 1. σ is almost independent of the pitch. The straight lines in Fig. 14 indicate the averages of the relative noise levels. They are 1.51, 1.20, 0.98, 0.82, 0.71, 0.47, and 0.34 for 0.6,

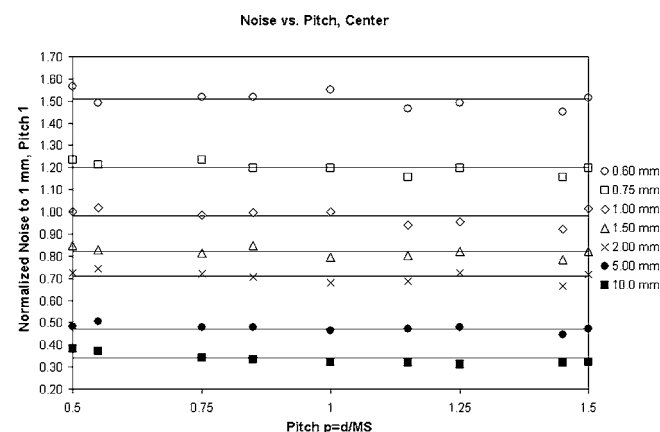


FIG. 14. Image noise σ in the center of a centered 20 cm water phantom for constant effective mAs as a function of the spiral pitch, for 0.6, 0.75, 1.0, 1.5, 2.0, 5, and 10 mm nominal slice-width. The image noise has been arbitrarily normalized to the value at 1 mm slice width and pitch 1. The lines are the calculated mean values. The image noise shows only slight variations as a function of the spiral pitch.

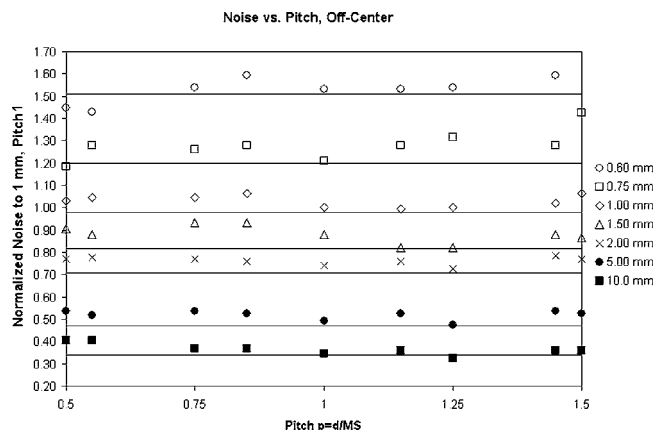


FIG. 15. Image noise σ at the periphery of a centered 20 cm water phantom for constant effective mAs as a function of the spiral pitch, for 0.6, 0.75, 1.0, 1.5, 2.0, 5, and 10 mm nominal slice width. Although fluctuations are somewhat larger, σ is still reasonably pitch-independent and corresponds very well to the noise in the center, see Fig. 14.

0.75, 1.0, 1.5, 2.0, 5, and 10 mm nominal slice width, respectively. These numbers can be compared to expected values obtained by calculating the square root of the ratios of the nominal slice widths

$$\sqrt{\frac{1}{0.6}} = 1.29, \quad \sqrt{\frac{1}{0.75}} = 1.16, \quad \sqrt{\frac{1}{1}} = 1.00,$$

$$\sqrt{\frac{1}{1.5}} = 0.82, \quad \sqrt{\frac{1}{2}} = 0.71, \quad \sqrt{\frac{1}{5}} = 0.45,$$

$$\sqrt{\frac{1}{10}} = 0.32.$$

The deviation between measured and expected values is less than 7% for all slice widths except 0.6 mm. In a simple model, image noise is expected to be inversely proportional to the square root of the FWHM of the respective SSPs. $\sigma\sqrt{\text{FWHM}}$ should therefore be a constant. Calculating

$\sigma\sqrt{\text{FWHM}}$ results in 1.17, 1.04, 0.98, 1.00, 1.00, 1.05, and 1.07 for 0.6, 0.75, 1.0, 1.5, 2.0, 5, and 10 mm nominal slice width, respectively. For the thinnest reconstructed slice, the measured image noise is 17% larger than expected with this simple model. The reason for the deviation between experimental and theoretically expected results is still under investigation.

In the CT scanner evaluated, the tube current mA is automatically decreased with decreasing pitch to compensate for the overlapping spiral acquisition. The radiation dose is therefore independent of the pitch. With decreasing pitch, more data are available for each image. This compensates the linear reduction of the tube current, and the image noise will be constant if all data are used for image reconstruction. The variation of σ of less than 7% as a function of the pitch demonstrates the correct utilization of the applied radiation dose at any pitch. Figure 15 shows the average image noise σ at the periphery of the centered 20 cm water phantom, again as a function of the spiral pitch. The average off-center noise levels are 1.55, 1.28, 1.03, 0.88, 0.76, 0.52, and 0.37 for 0.6, 0.75, 1.0, 1.5, 2.0, 5, and 10 mm nominal slice width. Although off-center noise shows somewhat larger fluctuations, it is still reasonably pitch-independent and corresponds very well to the noise in the center of the 20 cm water phantom.

D. Spiral image quality

Figures 16 and 17 show axial slices, MPRs, and the corresponding detail views as indicated by the white boxes, of the anthropomorphic thorax phantom at different pitch values. The ribs (arrow) are located 13 cm off-center, well within the “limiting” radius (see Sec. II B). In the axial slices there are no indications of spiral windmill-type artifacts at high contrast structures, the MPRs are free of streak artifacts. Image quality is independent of the pitch. This can be demonstrated by subtracting corresponding images acquired at pitch 0.5 and 1.5: the difference images mainly show noise and no structures. Figures 18 and 19 illustrate the influence

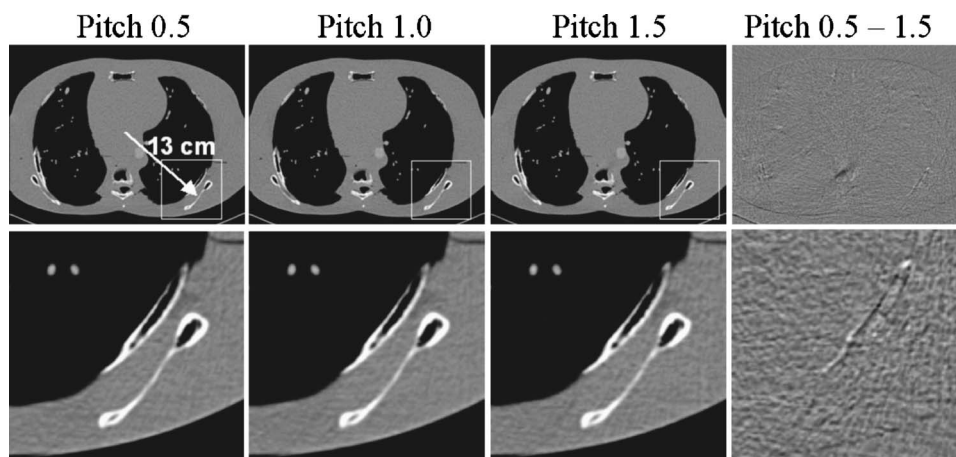


FIG. 16. Axial slices (top) and detail views (bottom) as indicated by the white boxes of an anthropomorphic thorax phantom at different pitch values. There are no indications of spiral windmill-type artifacts around high contrast structures. Image quality is independent of the pitch. Difference images mainly show noise and no structures.

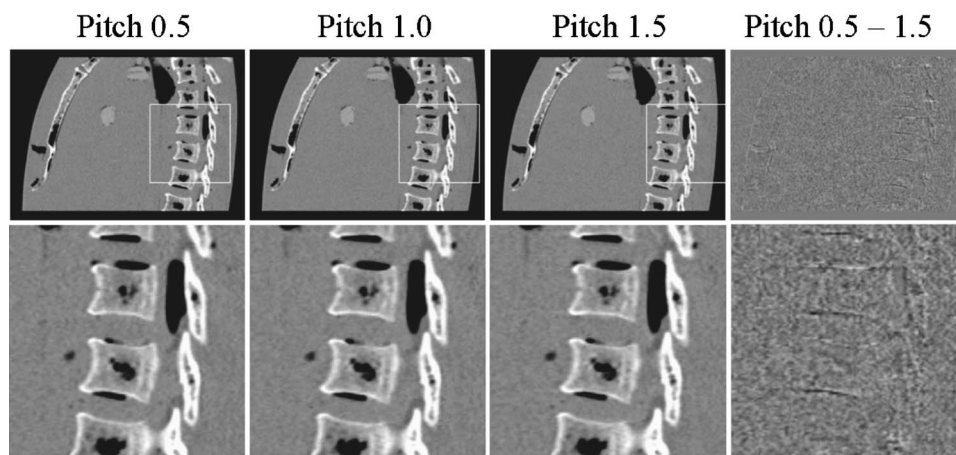


FIG. 17. Sagittal MPRs (top) and detail views (bottom) as indicated by the white boxes of an anthropomorphic thorax phantom at different pitch values. The MPRs are free of streak artifacts. Image quality is independent of the pitch. Difference images mainly show noise and no structures.

of the z-flying focal spot on spiral image quality for a patient example, a head and neck scan acquired at pitch 1.5. The images on the left were reconstructed with the original software available at the CT scanner investigated which supports the z-flying focal spot, the images on the right were reconstructed off-line with a modified approach considering only projections at one z position of the focal spot and hence neglecting the influence of the improved z sampling. The images without z-flying focal spot show severe windmill artifacts at inhomogeneous bone structures,¹¹ which are typical for MDCT head and neck scanning, may compromise clinical diagnosis, and hence limit the acceptance of spiral acquisitions in the head and neck.¹⁷ The image noise is increased compared to the original reconstructions because only half the measured projections (only one z position of the focal spot) are used for image reconstruction. Nevertheless, a comparison of the images with regard to artifacts is possible. With z-flying focal spot, spiral windmill artifacts are almost completely eliminated due to the improved z sampling. Fig-

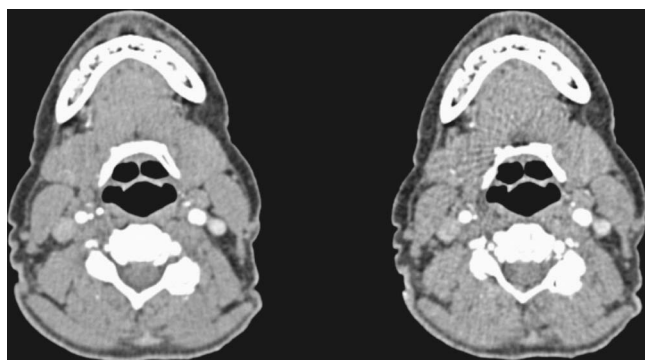


FIG. 18. Reduction of spiral artifacts with the z-flying focal spot technique. Left: neck scan with 32×0.6 collimation in a 64-slice acquisition mode with z-flying focal spot at pitch 1.5. Right: same scan, using only one focus position of the z-flying focal spot for image reconstruction. This corresponds reasonably well to evaluating 32-slice spiral data acquired without z-flying focal spot. Due to the improved longitudinal sampling with z-flying focal spot (left) spiral interpolation artifacts (windmill structures at high contrast objects) are suppressed without degradation of z-axis resolution.

ure 20 illustrates the influence of the z-flying focal spot on spiral image quality yet for another patient example with larger field of view, a thorax scan acquired at pitch 1.5. The sternum (arrow) is located approximately 12 cm off-center.

IV. DISCUSSION AND CONCLUSION

The z-flying focal spot technique is a novel concept to improve z sampling with MDCT systems. Simultaneous acquisition of 64 submillimeter slices using this technology allows pitch-independent increase of longitudinal resolution and suppression of spiral artifacts. The benefits of the z-flying focal spot technique are maintained within a “limiting” radius ($r_{lim}=180$ mm for the evaluated CT scanner), which corresponds well to the area of interest for the majority of medical CT applications. Other approaches attempt to improve z sampling by the choice of optimized small pitch values, so that complementary data acquired in different rotations interleave in the z direction.^{18,19} At these optimized pitches (e.g., 0.53 125 for 32-row detectors), longitudinal resolution comparable to the case with z-flying focal spot can be achieved by using narrow spiral interpolation functions. At higher pitches > 1 , however, longitudinal resolution degrades, which is avoided by the z-flying focal spot technique.

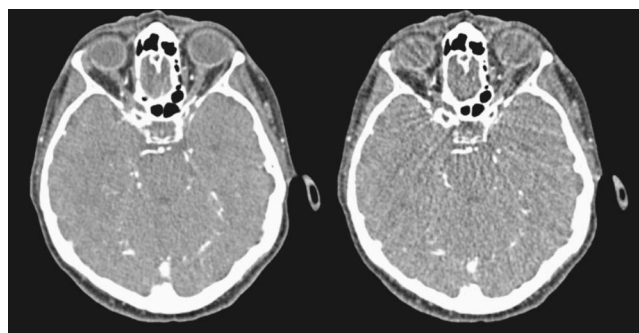


FIG. 19. Reduction of spiral artifacts with the z-flying focal spot technique (left) for a head scan, see Fig. 18 for a detailed explanation.

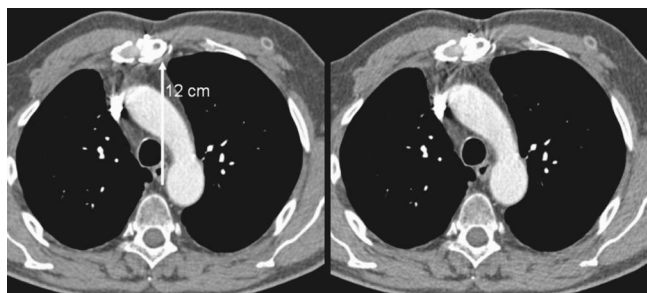


FIG. 20. Reduction of spiral artifacts with the z-flying focal spot technique (left) for a thorax scan with larger field of view, see Fig. 18 for a detailed explanation.

Furthermore, with those alternative approaches^{18,19} improved z sampling at optimized small pitch values is achieved close to iso-center only, see Fig. 21.

Other techniques to suppress spiral artifacts adopt the width of the spiral interpolation function to the local z gradient of the CT measurement data.²⁰ As a consequence thereof, local resolution in the vicinity of z-inhomogeneous objects will be degraded, which is avoided using the z-flying focal spot technique.

The CT scanner evaluated provides well-defined spiral SSPs with a minimum width of 0.66 mm, with only minor variations as a function of the spiral pitch, and enables the longitudinal resolution of centered objects down to 0.33 mm in size. 100 mm off-center, 0.36 mm objects can still be resolved. In contrast to conventional MDCT spiral scan and reconstruction approaches, spiral image quality is largely independent of the pitch. Using conventional MDCT systems, demanding applications such as neuro scanning require low pitch protocols to reduce artifacts and to improve image quality. CTAs of the carotid arteries and the circle of Willis

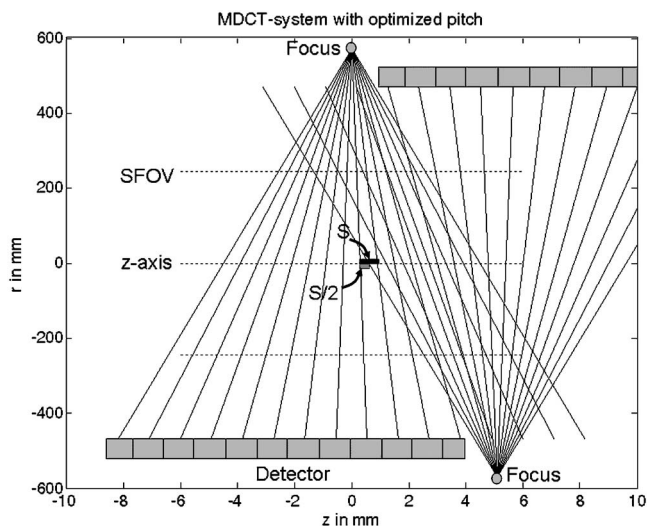


FIG. 21. Schematic illustration of an alternative method to improve z sampling, based on using optimized small pitch values, so that complementary data acquired in subsequent rotations interleave in the z-direction (compare to Fig. 2). Improved z sampling with sampling distance $S/2$, which allows the use of narrow spiral interpolation functions to increase longitudinal resolution, is achieved close to isocenter only.

for instance require a careful optimization of the spiral pitch to ensure high volume coverage speed on the one hand and to avoid intolerable spiral artifacts on the other. The z-flying focal spot technique maintains a low artifact level up to pitch 1.5, thus increasing the maximum volume coverage speed that can be clinically used. Selected clinical protocols relying on 32×0.6 mm collimation in a 64-slice acquisition mode using the z-flying focal spot may serve as examples. CTAs of the carotid arteries and the circle of Willis acquired at 0.33 s rotation time and pitch 1.5 require less than 5 s for a scan range of 350 mm, hence they can be acquired in the purely arterial phase. The entire thorax (400 mm) can be scanned at 0.5 s rotation time and pitch 1.4–1.5 in about 7 s, facilitating the examination of emergency patients, e.g., with suspicion of acute pulmonary embolism.

A whole-body submillimeter CTA with 1500 mm scan range, 0.37 s gantry rotation time, and pitch 1.2–1.4 will be completed in 22–25 s. Clinical experience will have to determine the full spectrum of new applications made possible by this new z-sampling concept for MDCT systems. Early experience has already demonstrated a substantial improvement in spatial resolution and artifact level in neuro CT,¹⁷ and increased diagnostic resolution of vascular anatomy and pathology in CT angiography.²¹

^{a)}Electronic mail: thomas.flohr@siemens.com

¹K. Klingenberg-Regn, S. Schaller, T. Flohr, B. Ohnesorge, A. F. Kopp, and U. Baum, "Subsecond multi-slice computed tomography: Basics and applications," *Eur. J. Radiol.* **31**, 110–124 (1999).

²H. Hu, H. D. He, W. D. Foley, and S. H. Fox, "Four multidetector-row helical CT: Image quality and volume coverage speed," *Radiology* **215**, 55–62 (2000).

³T. Fuchs, M. Kachelrieß, and W. A. Kalender, "Multi-slice spiral computed tomography: System performance and new applications," *IEEE Eng. Med. Biol. Mag.* **19**, 63–70 (2000).

⁴T. Flohr, K. Stierstorfer, H. Bruder, J. Simon, and S. Schaller, "New technical developments in multislice CT. 1. Approaching isotropic resolution with sub-mm 16-slice scanning," *Rofo Fortschr Geb Röntgenstr Neuen Bildgeb Verfahr* **174**, 839–845 (2002).

⁵B. Wintersperger, P. Herzog, T. Jakobs, M. Reiser, and C. Becker, "Initial experience with the clinical use of a 16 detector row CT system," *Crit. Rev. Comput. Tomogr.* **43**, 283–316 (2002).

⁶U. J. Schoepf et al., "Multislice CT angiography," *Eur. Radiol.* **13**, 1946–1961 (2003).

⁷W. A. Kalender, "Thin-section three-dimensional spiral CT: Is isotropic imaging possible?," *Radiology* **197**, 578–580 (1995).

⁸K. Nieman, F. Cademartiri, P. A. Lemos, R. Raaijmakers, P. M. T. Pattynama, and P. J. de Feyter, "Reliable noninvasive coronary angiography with fast submillimeter multislice spiral computed tomography," *Circulation* **106**, 2051–2054 (2002).

⁹D. Ropers et al., "Detection of coronary artery stenoses with thin-slice multi-detector row spiral computed tomography and multiplanar reconstruction," *Circulation* **107**, 664–666 (2003).

¹⁰T. Flohr, H. Bruder, K. Stierstorfer, and S. Schaller, "Evaluation of approaches to reduce spiral artifacts in multi-slice spiral CT," *Abstract Book of the 89th Scientific Assembly and Annual Meeting of the RSNA*, 2003, p. 567.

¹¹K. Taguchi, H. Aradate, Y. Saito, I. Zmora, K. S. Han, and M. D. Silver, "The cause of the artifact in 4-slice helical computed tomography," *Med. Phys.* **31**, 2033–2037 (2004).

¹²S. Schaller, K. Stierstorfer, H. Bruder, M. Kachelrieß, and T. Flohr, "Novel approximate approach for high-quality image reconstruction in helical cone beam CT at arbitrary pitch," *Proc. SPIE*, **4322**, 113–127 (2001).

¹³T. Flohr, K. Stierstorfer, H. Bruder, J. Simon, A. Polacin, and S. Schaller, "Image reconstruction and image quality evaluation for a 16-slice CT

- scanner,” *Med. Phys.* **30**, 832–845 (2003).
- ¹⁴G. Larson, C. Ruth, and C. Crawford, “Nutating slice CT image reconstruction,” Patent Application WO 98/44847, filed 8 April, 1998.
- ¹⁵M. Kachelrieß, S. Schaller, and W. A. Kalender, “Advanced single-slice rebinning in cone-beam spiral CT,” *Med. Phys.* **27**, 754–772 (2000).
- ¹⁶H. Bruder, M. Kachelrieß, S. Schaller, K. Stierstorfer, and T. Flohr, “Single-slice rebinning reconstruction in spiral cone-beam computed tomography,” *IEEE Trans. Med. Imaging* **19**, 873–887 (2000).
- ¹⁷C. H. McCollough, E. P. Lindell, A. N. Primak, J. G. Fletcher, K. Stierstorfer, and T. G. Flohr, “Early experience with 64-slice CT and Z-axis oversampling: Novel applications and the elimination of helical artifacts in neuro CT,” On-line Abstract Book of the 90th Scientific Assembly and Annual Meeting of the RSNA, 2004.
- ¹⁸H. Hu, “Multi-slice helical CT: Scan and reconstruction,” *Med. Phys.* **26**, 5–18 (1999).
- ¹⁹J. Hsieh, “Analytical models for multi-slice helical CT performance parameters,” *Med. Phys.* **30**, 169–178 (2003).
- ²⁰J. Hsieh, “Adaptive interpolation approach for multi-slice helical CT reconstruction,” *Proc. SPIE* **5032**, 1876–1883 (2003).
- ²¹T. R. Vrtiska, J. G. Fletcher, and C. H. McCollough, “State-of-the-art imaging with 64-channel multidetector CT-angiography,” *Perspectives Surgery Endovascular* **17**, 3–8 (2005).